

Hole-doping structural titration and manipulation of correlated charge density wave state in 1T-TaS₂

Haoyu Dong^{1,2,+}, Yanyan Geng^{1,2,+}, Jianfeng Guo^{1,2}, Le Lei^{1,2}, Manyu Wang^{1,2}, Yan Li³, Li Huang³, Fei Pang^{1,2}, Rui Xu^{1,2}, Wei Ji^{1,2}, Hong-Jun Gao³, Weichang Zhou^{4,*}, and Zhihai Cheng^{1,2,*}

¹*Beijing Key Laboratory of Optoelectronic Functional Materials & Micro-nano Devices, Department of Physics, Renmin University of China, Beijing 100872, China*

²*Key Laboratory of Quantum State Construction and Manipulation (Ministry of Education), Renmin University of China, Beijing, 100872, China*

³*Beijing National Laboratory for Condensed Matter Physics, Institute of Physics, Chinese Academy of Sciences, Beijing 100190, China*

⁴*Key Laboratory of Low-dimensional Quantum Structures and Quantum Control of Ministry of Education, School of Physics and Electronics, Institute of Interdisciplinary Studies, Hunan Normal University, Changsha 410081, China*

Abstract: The complex correlated charge density wave (CDW) phases of 1T-TaS₂ have attracted a lot of interest due to their emergent quantum states, such as intricate CDW phase, Mott-Hubbard state, superconductivity and quantum spin liquid state. The delicate interplay among the complex intra-/inter-layer electron-electron and electron-lattice interactions is the fundamental prerequisite for these exotic quantum states. Here, we report a real-space titration-like investigation of correlated CDW state in 1T-TaS₂ upon hole-doping via variable-temperature scanning tunneling microscope (VT-STM). The sequential increased hole-doping result in the emergence of electron voids, phase domains, stacking disordering and mixed phase/chiral domains due to the gradual weaken electron correlations. The detailed configurations and dynamic behaviors of these features as well as novel ring-Star-of-David (SoD) clusters and stripe-like nematic CDW state are further investigated and discussed based on the complex structural-sensitive interactions. The local reversible disordering-ordering CDW manipulation is further realized by the transient charge-injections via the field-emission bias-pulses. Our results provide an in-depth insight of this delicate correlated CDW states, and pave a way to realize exotic quantum states via the accurate tuning of interior interactions in correlated materials.

⁺These authors contributed equally: Haoyu Dong, Yanyan Geng

^{*}Email: zhahaicheng@ruc.edu.cn, wchangzhou@hunnu.edu.cn

Introduction

TMD and CDW, superconductivity, etc.

Transition metal dichalcogenides (TMDs) of the MX_2 type, where M represents the metal and X denotes the chalcogens, have garnered significant attention from physicists since their structures were first proposed [1-3]. TMDs exhibit a wide range of intriguing physical properties arising from their intricate electron-electron, electron-phonon interactions and interlayer coupling [4-8]. TMDs offer an extensive platform for fundamental investigations of interactions, such as exploring charge density waves (CDW) and quantum spin liquid in materials like TaS_2 , $TaSe_2$, $NbSe_2$ and unconventional superconductivity in materials like $TaSe_2$ and MoS_2 , as reported in recent studies [9-13]. These TMDs with diverse band structures play a crucial role in both fundamental research and practical applications.

1T-TaS₂ CDW and exotic quantum states

Among the TMD materials, 1T-TaS₂ has evoked great interest due to its unique Mott-insulator nature combined with a CDW, which undergoes a commensurate CDW transition at approximately 180 K, as shown in Supplementary Fig. 1 [9-11]. In this commensurate CDW state of 1T-TaS₂, the in-plane lattice distortion leads to the formation of Star of David (SoD) clusters comprising 13 Ta atoms, each hosting an unpaired electron. Further band structure calculations suggest that these unpaired electrons within the SoD clusters form a narrow electronic band that may be susceptible to the Mott-Hubbard transition induced by in-plane Coulomb interaction. Within this Mott insulating state, this localized unpaired electron manifests as an effective spin-1/2 local magnetic moment. No conventional magnetic ordering has been observed in 1T-TaS₂ down to millikelvin temperatures, thus proposing it as a potential spin-1/2 triangular lattice quantum spin liquid candidate [14-17]. Recent research also shows the appearance of a series of low-temperature electronic states in 1T-TaS₂ with pressure, finding a superconductivity state develops within the CDW state, and survives to very high pressures, insensitive to subsequent disappearance of the CDW state and also the strong changes in the normal state [11].

Complex CDW phase and chiral configurations and interactions in 1T-TaS₂

The lattice periodic modulations and e-e/e-ph interactions in CCDW 1T-TaS₂ at low temperatures gives rise to the formation of different electron domain wall (DW) configuration,

which have been extensively observed. These phases and chiral DWs, significantly have influence on the electronic and topologically state of $1T\text{-TaS}_2$, which have been reported by experimental and theoretical investigations [18-33], thus represent a key focus in this field of research. Both phase and chiral domains lead to variations in interlayer stacking order and diverse electronic states within SoD superlattices, as recently reported for $1T\text{-TaS}_2$ and $1T\text{-TaSe}_2$ [8,34-41]. Furthermore, the electronic states of CDW have been controlled by various techniques, such as ultrafast laser pulse excitation as reported recently [42-46]. It is also an intriguing idea to realize the real-space localized modulation or reversible manipulation of CDW electronic states, which may pave a way to realize exotic quantum states via the accurate modulation.

In this work, we report a real-space investigation of correlated interactions in the CDW state of $1T\text{-TaS}_2$ by titration-like hole-doping via variable-temperature STM. With the increased hole-doping and weakened electron-electron correlations, sequential emergence of electron voids, phase domains, stacking disorder, and mixed phase/chiral domains is observed in $1T\text{-TaS}_2$, which gradually decrease in size as the hole-doping increased. Phase domains are found throughout the sample, leading to variations interlayer stacking and resulting in a step-like features in STM images. With increased hole-doping, chiral DWs appear within layers while interlayer bonding fails to homogenize the chirality between upper and lower layers. A novel ring-SoD cluster and stripe-like nematic CDW state are observed and discussed via STM measurements and atomic structure schematic. Additionally, reversible local manipulation of CDW ordering-disordering through transient charge injections via field-emission bias-pulses allows for the control of CDW order. Our research not only enhances the understanding of correlated electrons but also pave a way to realize exotic quantum states via the accurate modulation of interactions in correlated electron materials.

Results and discussion

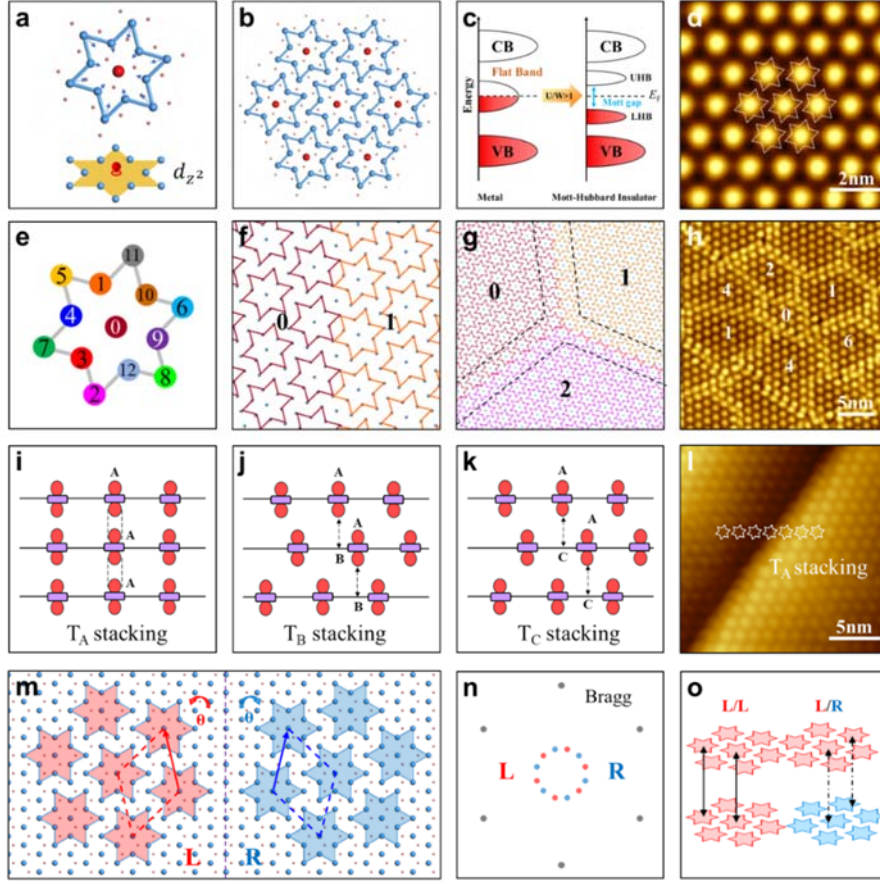


Figure 1. Atomic and electronic structure of the correlated CDW state in 1T-TaS₂. (a) Atomic models of the Star of David (SoD) cluster with the maximally localized d_{z^2} orbital (unpaired electron) of the central Ta atom in top and oblique view. (b) Schematic illustration of the SoD clusters with the commensurate $\sqrt{13} \times \sqrt{13}$ periodicity. (c) Schematic electronic band structures of correlated CDW state, in which the half-filled flat band of the localized d_{z^2} orbital is split into the UHB and LHB bands via the electron correlation effect. (d) STM image of commensurate CDW state with the overlaid SoD models. $V=0.4\text{V}$, $I=100\text{pA}$. (e,f) Atomic Ta-indexed model (e) of the SoD cluster for the definition of CDW phase domain wall (DW, f). A DW is defined as the center of SoD cluster of the neighboring domain sits on Ta atomic sites of 1-12, as shown by the example of DW-1 in (f). (g) Schematic illustration of a vortex consisting of three type DWs. (h) Typical STM image of metastable mosaic CDW state induced by STM bias-pulse. $V=0.6\text{V}$, $I=100\text{pA}$. (i-k) Schematic illustrations for the interlayer T_A (i), T_B (j), and T_C (k) phase stacking of correlated CDW state with the marked central half-filled state of SoDs. The interlayer T_A , T_B and T_C stacking were defined by the out-of-plane alignment of Ta-0, Ta-1,3,4,9,10,12 and Ta-2,5,6,7,8,11 defined in (e), respectively. (l) STM image of a step edge showing the common T_A stacking in 1T-TaS₂. $V=0.6\text{V}$, $I=100\text{pA}$. (m) Schematic of the L- and R-chiral CDW phases marked by red and blue stars, respectively. The mirror-symmetric L- and R- SoD superlattices were marked by dashed lines. (n) Schematic FFT pattern of L- and R- CDW domains with the atomic Bragg spots. (o) Schematic of the interlayer homochiral and heterochiral stackings.

Correlated CDW state

The ground CCDW state of 1T-TaS₂ consists of the commensurate $\sqrt{13}\times\sqrt{13}$ superlattice of SoD clusters, as shown in Fig. **1a-b**. The SoD cluster is made of 12 inward-distorted outer and one center Ta atoms, in which the twelve $5d_{z^2}$ electrons of the outer Ta atoms pair and form six occupied CDW valence bands. The remaining one unpaired electron of SoD is maximally localized at the central Ta atom to form the half-filled flat band, which is further split into the upper Hubbard band (UHB) and lower Hubbard band (LHB) bands due to the strong intralayer electron-electron correlations (Fig. **1c**). Fig. **1d** shows the STM image of the correlated CDW state with the overlaid star models of SoDs.

Phase domains and domain walls

The superlattice structure of correlated CDW in 1T-TaS₂ with the underlying atomic lattice can lead to the formation of 13 phase domains separated by 12 different DWs, as shown in Fig. **1e-h**. The different phase domains and DWs can be defined by the relative positions of the central Ta atoms in the neighboring phase domains. The SoDs of 12 phase DWs show various overlapping structural configurations and stabilities (Supplementary Fig. 2) [20]. The crossing of three straight phase DWs can further form the CDW vortex structures (Fig. **1g**). In contrast to the stable ground CCDW state, the above metastable states can be introduced by STM bias-pulse, and laser pulse to form the mosaic state (local metastable hidden state) [20-24]. Fig. **1h** shows the STM image of the bias-pulse-induced mosaic state, which consist of various phase CDW domains, DWs and CDW vortexes.

Interlayer stacking configurations

The superlattice structure of correlated CDW with the underlying atomic lattice can also lead to the more complex interlayer stacking configurations. The three typical interface stacking of T_A, T_B and T_C are defined by the out-of-plane alignment of central Ta atoms in the neighboring layers and schematically shown in Fig. **1i-k**. Figure **1l** shows the STM image of the most common and stable T_A stacking configurations confirmed by the overlaid SoD models across the step edges. It is noted that, in the T_A stacking configuration, the central local half-filled d_{z^2} orbitals of interfacial neighboring SoDs can hybridize into the trivial spin-paired dimerized band insulating state in competition with the intralayer Mott-Hubbard insulating state [34-41]. The interlayer hybridization was proven to decrease during the

thermal fluctuations at elevated temperatures [20].

Chiral CDW domains

The $\sqrt{13}\times\sqrt{13}$ superlattice structure of SoDs with the underlying atomic lattice can also lead to the two kinds of mirror-symmetric chiral CDW domains, as shown in Fig. **1m-o**. In the L- and R- domains, the SoD superlattices are rotated clockwise by -13.9° and $+13.9^\circ$ from the Ta lattice, respectively. In general, the lateral size of the $\sqrt{13}\times\sqrt{13}$ domain of a SoD superlattice in $1T\text{-TaS}_2$ is much larger than normal scan range of STM measurements of about a few hundred nanometers [5], and their interlayer stackings are almost exclusively preferred to the homochiral stacking even in different phase stacking configurations. Only very few works about the chiral CDW state were just reported recently with the focus on their global chiral switching via the circularly polarized light or electrical pulse in the nanothick flakes [42-43]. The heterochiral CDW DWs and stacking configurations are shown in Supplementary Fig. 3 and rarely investigated. The heterochiral overlapping (intralayer) or stacking (interlayer) of CDW domains could form a super-superlattice of 13×13 ($\sqrt{13}\times\sqrt{13}$) with respect to the underlying atomic (SoD) lattice.

Hole-doping structural titrations

In the pristine $1T\text{-TaS}_2$, the formation of the perfect commensurate CDW state is from the interplay/competition of intralayer and interlayer interactions, including the electron-electron correlations and electron-lattice couplings. The enhanced thermal fluctuations at elevated temperatures can adjust the delicate interplay of these complexed interactions to form a series of CDW phases. The charge-doping effects in $1T\text{-TaS}_2$ have been discussed in different ways, including the emergent superconductivity of copper-intercalated bulks and gate-tunable nanothick flakes, which may also affect atomic structure (Supplementary Fig. 4) [29-30]. It is very promising and important to further investigate the electron-filling-dependent CDW states with the focus on their complicated CDW intralayer and interlayer configurations and interactions in a titration-like way, as shown in Supplementary Fig. 5-6. The electron-filling of flat band in correlated CDW state can be gradually reduced by controllable hole-doping in the Ti-doped $1T\text{-Ta}_{1-x}\text{Ti}_x\text{S}_2$ [47], which is investigated in our following work.

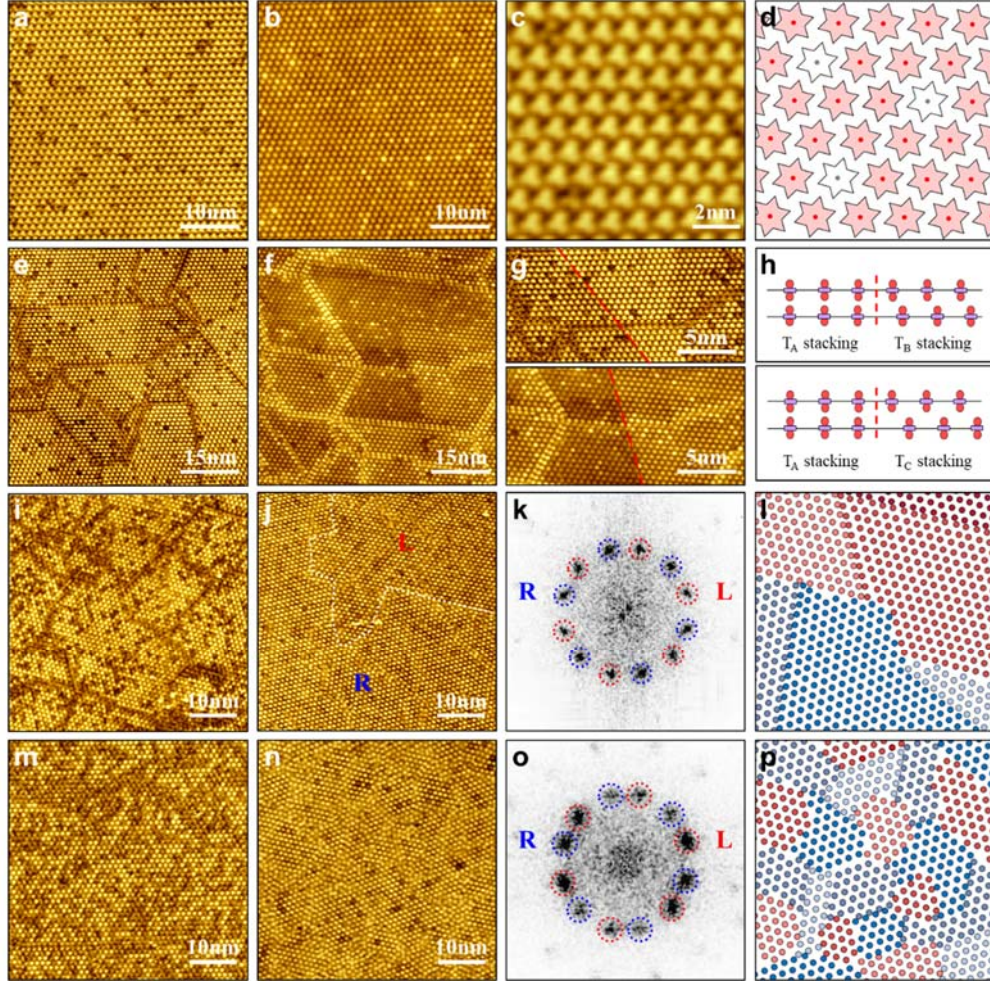


Figure 2. STM measurements of sequential structural titration in hole-doped 1T-TaS₂. (a-d) Large-scale occupied state (a), unoccupied state (b) and high-resolution (c) STM images of tiny-hole-doped 1T-TaS₂, and their schematic model (d). The central electron-filled and -empty SoDs are marked by the central red and grey dots, respectively. (e-h) Large-scale occupied state (e), unoccupied state (f) and high-resolution (g) STM images of mosaic-like low-hole-doped 1T-TaS₂, and the possible stacking models (h). The step-like features of top layer are due to the different stacking order via the phase domains in the underlying bottom layers, as schematically shown by the dashed lines of underlying DWs in (g,h). (i-l) Large-scale occupied state (i), unoccupied state (j) STM images and their typical FFT pattern (k) of medium-hole-doped 1T-TaS₂, and their structural model (l). The emergent large chiral CDW domain is made of many small homochiral phase domains. The L- and R- chiral domains are separated by white dotted lines in (j), and schematically illustrated in (l). (m-p) Large-scale occupied state (m), unoccupied state (n) STM images and their typical FFT pattern (o) of high-hole-doped 1T-TaS₂, and their structural model (p). The fragmented CDW state is made of randomly distributed tiny phase and chiral domains, schematically illustrated in (p). Scanning parameter of occupied state: $V = -0.4V$, $I = -100pA$; unoccupied state: $V = 0.4V$, $I = 100pA$.

Distributed void SoDs

At the tiny-hole-doped level, as shown in the STM images of Fig. 2a and b, the discretely distribution electron-void SoDs emergent within the commensurate SoD superlattice, showing darker (brighter) contrast than the normal SoDs at the occupied (unoccupied) state. These void SoDs without the central localized electrons are clearly resolved as the darker clover shapes in the high-resolution STM image of Fig. 2c, and further schematically illustrated in Fig. 2d. The discretely distribution of individual void SoDs is also consistent with the repulsive electron-electron correlations of partial-filled flat-band in the correlated CDW state. The atomic-resolved AFM measurements have been performed to confirm the electron-void nature of these emergent clover-shaped SoDs at the tiny-hole-doped level.

Phase domains & stacking configurations

At the low-hole-doped level, as shown in the STM images of Fig. 2e and f, the mosaic-like CDW states are observed with the emergent phase domains and DWs, which is in general similar with the pulse-induced metastable mosaic CDW state in pristine 1T-TaS₂. It is noted the mosaic-like CDW states are the stable ground state in the thermal equilibrium, which is existent in each layer due to the hole-doping and different from the metastable (by the external energy excitations) mosaic state of surface layers. The decreased intralayer electron-electron correlations is not enough to sustain the long-range phase ordering of correlated CDW state at the low-hole-doped level. In addition, the consequent various local interlayer stacking configurations further contribute the complexity of these mosaic-like CDW states, such as the marked step-like intra-domain features (Fig. 2g), which should be due to the DWs on the underlying bottom layer (Fig. 2h). The stacking-sensitive interlayer hybridizations led to the different apparent contrasts in the surface-sensitive STM images.

Chiral CDW domains

At the medium-hole-doped level, as shown in the STM images of Fig. 2i and 2j, the mosaic-like CDW states can still be observed, while no apparent stacking-sensitive contrast is resolved in the STM measurements due to the further reduction of interlayer electronic hybridizations. In addition, the large chiral CDW domains emergent within the mosaic-like CDW states, as shown by the marked chiral DWs to separate the R- and L- chiral domains in

Fig. 2j and the corresponding FFT pattern of Fig. 2k. The large chiral domains are made of many small homochiral phase domains, as schematically illustrated in Fig. 2l. It is also noted that, different from the DWs at low-doped-level, the DWs of Fig. 2i and 2j could not be readily resolved based on their specific local contrast. These results indicate that the further decreased electron-electron correlations are not enough to sustain the chiral ordering of correlated state at the medium-hole-doped level.

Mixed phase and chiral domains

At the high-hole-doped level, as shown in the STM images of Fig. 2m and 2n, the fragmented CDW states are observed, which is made of randomly distributed tiny phase and chiral domains. The short phase and chiral DWs are disordered and could not be clearly defined, consistent with the faint electron-electron correlations. The FFT pattern of Fig. 2o is generally similar to that of Fig. 2k but with more blurred and diffused FFT spots, representing the heavily disrupted CDW phase and chiral domains illustrated in Fig. 2p. More images of sequential structural titration in hole-doped 1T-TaS₂ were shown in Supplementary Fig. 7.

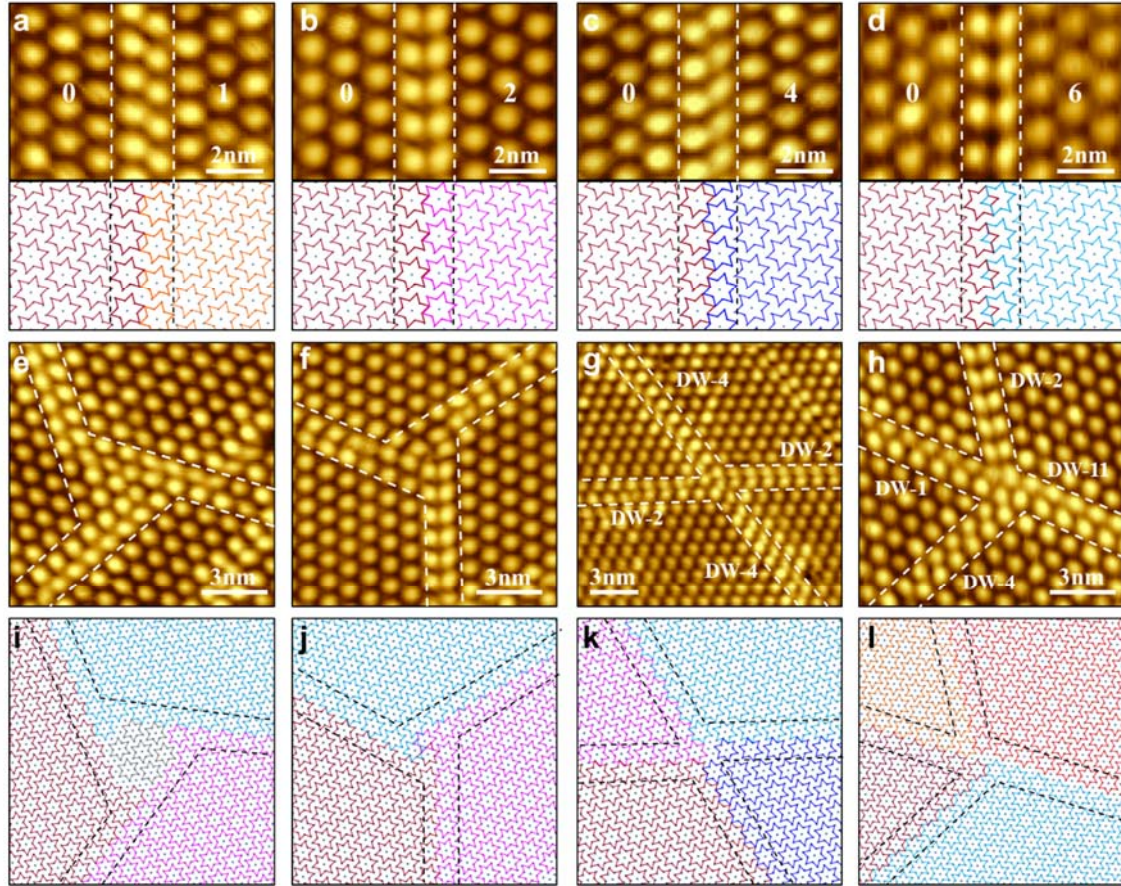


Figure 3. Intralayer phase DWs and CDW vortex of low-hole-doped 1T-TaS₂. (a-d) STM images of four typical CDW phase DWs (top) and their schematic structural configurations (bottom). The constituent SoDs of phase DWs are highlighted by the dashed lines separating the two marked neighboring phase domains. The overlap between the SoDs of DWs in (a-d) gradually increases, leading to reduced structural stability as a result of stronger inter-SoD repulsive interactions. (e-l) STM images of four typical CDW vortices and their schematic structural configurations (i-l). The constituent SoDs of phase DWs and CDW vortices are highlighted by the dotted lines separating the three/four marked CDW phase domains. STM images were taken under the tunneling condition $V=0.4\text{V}$, $I=100\text{pA}$.

Phase domain walls and vortex

Figure 3**a-d** show the STM images of four emergent phase DWs in the low-hole-doped 1T-TaS₂, in which the DWs of 3**a** and 3**b** are frequently observed. While the DWs of 3**c** and 3**d** could only be occasionally and rarely observed in STM experiments. It is noted that the SoDs of DWs in 3**a-d** shows gradual increased overlaps, consistent with their gradual reduced proportions. It can be concluded that the overlap-dependent inter-SoD repulsive electron correlations determine the different structural stabilities of DWs, the larger overlap, the less structural stability. These observed DWs in the thermal stable mosaic-like CDW state of low-hole-doped 1T-TaS₂ is generally consistent with those in the pulse-induced metastable mosaic state of pristine 1T-TaS₂, while the latter can be recovered into the perfect commensurate CDW state at elevated temperatures (Supplementary Fig. 8) [20]. Fig. 3**e-h** show the STM images of four emergent CDW vortexes in the low-hole-doped 1T-TaS₂, in which the two three-fold symmetric chiral CDW vortexes of 3**e**,3**f** are made of three stable DWs of 3**a**,3**b** respectively. Fig. 3**g** shows the intersection of DW-2 and DW-4 with the symmetric shifting in both DWs, resulting in the formation of a chiral 4-vortex. More irregular CDW vortexes were also observed in the mosaic-like CDW state, such as the 4-vortex of Fig. 3**h**, which is the cross intersection of four different DWs.

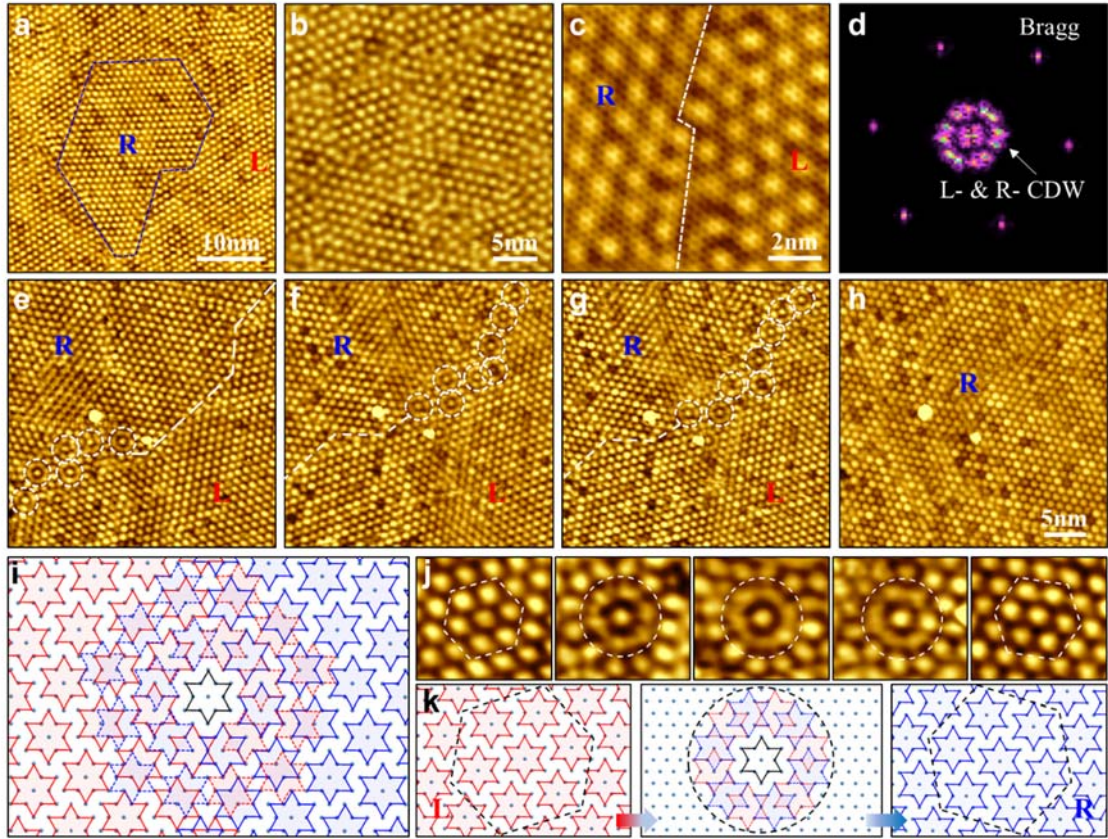


Figure 4. Intralayer chiral DWs and chirality-switching transition of hole-doped 1T-TaS₂. (a,b) STM images of large chiral domains (a) and mixed chiral/phase domains (b). The chiral DW is along the R-chirality (110) SoD direction and marked by blue dashed lines. (c,d) Atomic-resolution STM image (c) of typical chiral DWs and its corresponding FFT image pattern (d) with marked Bragg and chiral CDW spots. The chiral DW is marked by white dashed lines. (e-h) A sequential in-situ STM images showing the intermediate ring-SoD clusters and the dynamic chiral-switching at the chiral DWs. The dynamic intermediate ring-SoD clusters are marked with the dashed circles. (i) Chiral SoD-overlapping model of the mirror-symmetric DW with the centered achiral SoD. (j,k) A series of selected STM images (j) showing the dynamic chirality-switching transition via the transient ring-SoD clusters and the proposed configuration models (k). STM images were taken under the tunneling condition $V= 0.4V$, $I= 100pA$.

Chiral domains walls

In the large chiral CDW domain state, a predominant chirality such as L- chirality in Fig. 4a can be identified with a more stable chiral DW aligned with the (110) direction of R- chirality's SoD (Supplementary Fig. 9). While in the mixed chiral/phase domains state of Fig. 4b, the chiral DWs is complex and include metastable mirror-symmetric chiral DWs, leading to a question that whether these DWs are induced by atomic defects. Then the STM characterization was performed in a special tip condition shows both atomic resolution and SoD electron resolution, as depicted in Fig. 4c, which indicate a defect-free atomic lattice at chiral DW. Additionally, the corresponding FFT image in Fig. 4d clearly exhibits two distinct lattice signals: the atomic lattice signal and L- /R- chirality CDW lattice signal in the middle. These results show that the SoD superlattice persists near the DW while the long-range periodicity breaks, indicating that short-range neighboring electron-phonon interactions play a nonnegligible role in the formation of SoD.

Emergent and dynamic ring-SoD clusters

Then, the temperature was raised to 50K in order to investigate the dynamic change of metastable mirror-symmetric chiral DWs by in-situ STM characterizations (identified by bright spots), as depicted in Fig. 4e-h. A series of novel ring-shaped structures emerged and marked by dashed white circles, which aggregated specifically at the chiral DWs and named as “ring-SoD cluster”. The ring-SoD clusters and two chiral domains are observed to change over time, the R chiral domains expand while the L chiral domains diminish gradually until all eventually transform into R chiral (Fig. 4h), indicating the ring-SoD clusters are the dynamic intermediate electronic states of SoDs from one chirality to another (Supplementary Fig. 10).

These ring-SoD clusters at chiral DW consist of a central SoD surrounded by a non-chirality ring structure, which shows both L- and R- chirality [48]. An atomic structure model was shown in Fig. 4i to describe the hypothetical structure of this intermediate ring-SoD cluster with overlapping of two chirality SoDs, which features a unique central SoD that exhibits both L- and R- chirality (in other words, without chirality). Fig. 4j shows a series of selected STM images to demonstrate the procession of dynamic chirality transition via the intermediate ring-SoD clusters, with the atomic structure of Fig. 4k (Supplementary

Fig. 11). The emergence of local ring-SoD clusters indicates the effect of short-range neighboring interaction.

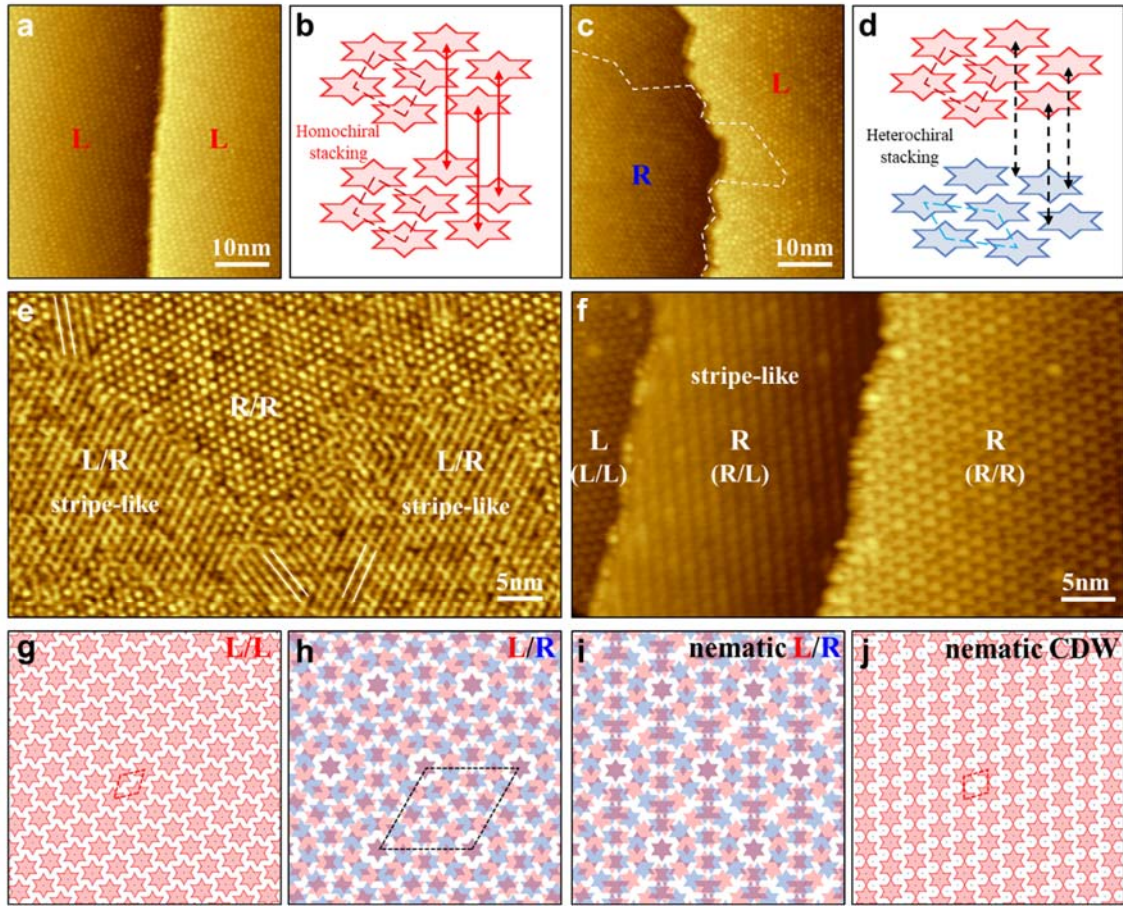


Figure 5. Interlayer chiral domain stacking and the emergent stripe-like pattern of hole-doped 1T-TaS₂. (a,b) STM images of step edges showing the homochiral stacking (a) and its schematic models (b). $V = -0.4\text{V}$, $I = -100\text{pA}$. (c,d) STM images of step edges showing the coexistent homochiral/heterochiral stacking (c) and the schematic model of heterochiral stacking (d). $V = -0.4\text{V}$, $I = -100\text{pA}$. (e) STM image of the chiral domain states with the emergent stripe-like pattern due to heterochiral stacking configuration. $V = 0.4\text{V}$, $I = 100\text{pA}$. (f) STM image of two step edges with specific homochiral/heterochiral stacking configurations and accompanying stripe-like feature. $V = -0.4\text{V}$, $I = -100\text{pA}$. (g,h) Top-view illustrations of homochiral (g) and heterochiral (h) stacking superstructures. (i) Possible directional relaxed heterochiral stacking configurations for the observed stripe-like pattern of nematic L/R stacking. (j) Proposed structural model of the stripe-like nematic CDW state.

Interlayer homo- and hetero-chiral stacking

The interlayer interaction was then analyzed by investigating the steps in tiny- and medium-hole-doped 1T-TaS₂. At tiny-hole-doped levels in Fig. 5a, there are no distinct chiral domains observed in both the upper and lower layers, shows a behavior of homochiral stacking (Fig. 5b), which is consistent with pristine 1T-TaS₂. Two distinct chiral domains emerge simultaneously within both the upper and lower layers in medium-hole-doped level in Fig. 5c, while the chirality between the upper and lower layers becomes irrelevant, causing a possibility of heterochiral stacking as shown in Fig. 5d. The decrease of electron filling weakens the interlayer electron-electron bonding, which fails to maintain consistent chirality between upper and lower layers.

Heterochiral stacking nematic CDW state

A novel dynamic stripe-like feature was observed immediately after the emergence of the intermediate ring-SoD clusters at elevated temperatures, which shows different directions (Fig. 5e). These stripe-like features along the (211) atomic structure direction are named as “nematic CDW” state and induced by interlayer heterochiral stacking configuration, which is demonstrated by homochiral and heterochiral stacking edges in Fig. 5f (Supplementary Fig. 12). The possible formation mechanism of the nematic CDW state can be explained by the schematic diagram in Fig. 5g-j. Different from the homochiral stacking configuration L/L (Fig. 5g), the heterochiral stacking configuration L/R (Fig. 5h) shows a larger and unstable super-superlattice of 13×13 ($\sqrt{13} \times \sqrt{13}$) with respect to the underlying atomic (SoD) lattice. The heterochiral stacking super-superlattice will undergo relaxation to achieve a relative stable nematic L/R structure, as illustrated in Fig. 5i. The proposed atomic structure is shown in Fig. 5j, which is intriguing and worthy of further study.

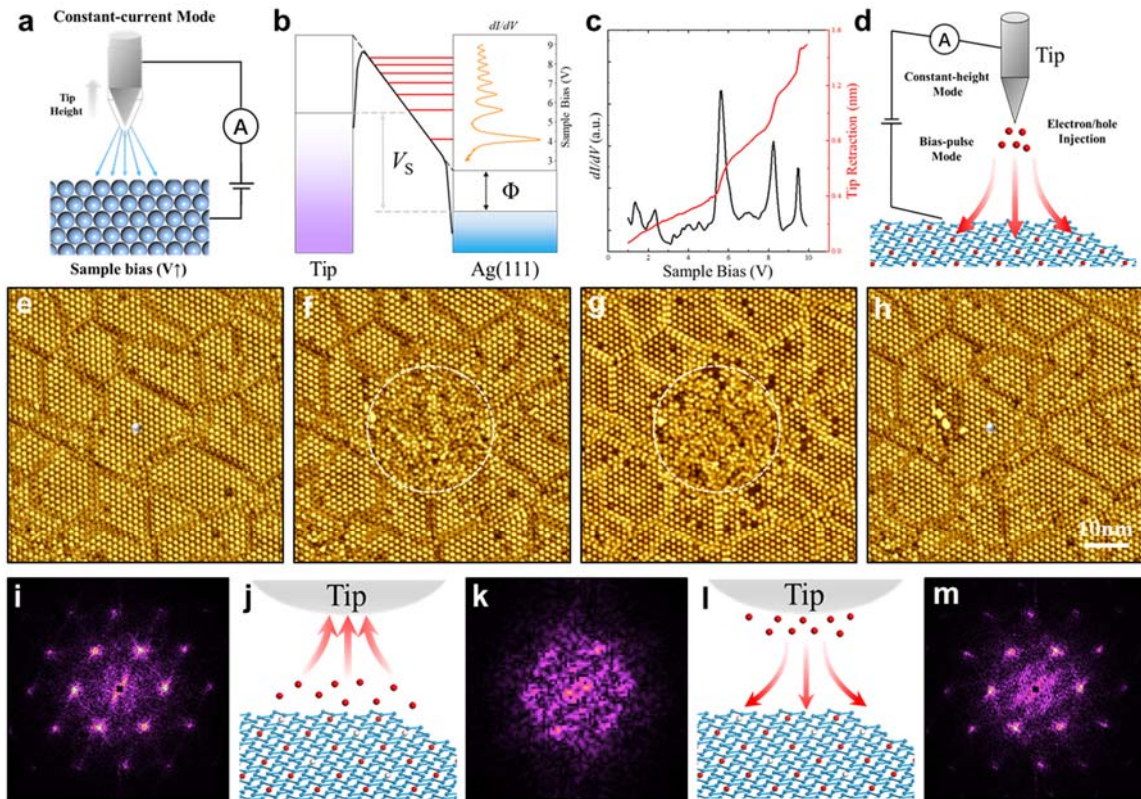


Figure 6. Local reversible manipulation of correlated CDW state in 1T-TaS₂ by field-emission-induced charge injection. (a) Schematic for the STM-based field emission resonance (FER) spectra measurement in constant-current mode. (b) FER spectra taken on Ag(111). (c) FER spectra of the correlated CDW state *i*. (d) Cartoon illustration for the field-emission-induced transient electron- and hole-injection. (e-h) STM images of correlated CDW state before (e) and after (f, g) transient hole-injection, and the reordered CDW state (h) by transient electron-injection. (i-m) The corresponding FFT pattern (i, k, m) and transient charge-inject cartoons (j, l) are sequentially illustrated. Scanning parameter are: (e, f, h) $V = -0.5\text{V}$, $I = -100\text{pA}$; (g) $V = 0.5\text{V}$, $I = 100\text{pA}$.

Discussion

Our study demonstrates the effect of electron-electron interactions, electron-phonon interactions, and interlayer interactions on the correlated CDW electrons in $1T$ -TaS₂ by introducing structural titration hole-doping and analyzing sequential emergent features of electron voids, phase domains, stacking disordering and mixed phase/chiral domains. As the electron filling decreases, the intralayer correlation interaction and interlayer bonding weakens, leading to intralayer phase/chiral DWs and inconsistent interlayer phase/chiral stacking configurations. These abundant correlation interactions and spontaneous formation of electronic states possess significant research value, making it imperative to explore methods for artificially modulate these correlation states.

Local reversible CDW manipulation

We then attempt to modulate the real-space correlation electrons by field emission [49-53] rather than tunneling effect, which can affect a large area of SoDs as shown in Fig. 6a. As schematically illustrated in Figure 6b, in field emission resonances (FERs), the bias voltage drops across the tunneling junction creates a trapezoidal potential. As their energies depend on local work function of sample, FER have been widely used in STM to determine sample's work function, as the FER result of $1T$ -TaS₂ in Fig 6c shows a work function of 5.5 eV. It is interesting to manipulate the CDW order by localized hole-injection and electron-injection in SoDs via constant-height mode field emission pulse, as shown by schematic in Fig. 6d. The charge-injection by field-emission bias-pulse was performed at a mosaic-like state of Fig. 6e. The application of a -6V (+6V) voltage bias-pulse at the central position induces disordered electron phase (recovered ordered CDW state) in the SoDs within the pulsed region shown in Fig. 6e-h, indicating the entropy increasing (decreasing) caused by the transient hole-(electron-) injection CDW manipulation and the realization of local reversible CDW phase transition manipulation (Supplementary Fig. 13). The corresponding FFT and charge-injection cartoons are shown in Fig. 6i-m, showing a blurry FFT pattern (Fig. 6k) of the disordered CDW state, indicating that the transient hole-injection will affect the valance band and conductive band, resulting in the mix of three bands (Supplementary Fig. 14), causing a disordered state similar like the quantum jamming state induced by a single laser pulse [46].

We have preliminarily attempted to employ hole-doping as a means of modulating the electron filling and electron-electron interaction in this research, further investigation into alternative methods is also worthy of study. For instance, investigating the possibility of extra-electron feature through electron-doping and exploring the corresponding properties represents a captivating and significant research area. Also, the present study demonstrates that the 4H_b structure of TaS₂ exhibits an alternating arrangement of T phase and H phase, resulting in a negligible interlayer interaction, which offering another exotic playground for hole-doping [54]. In addition, by introducing more hole-doping, it becomes possible to explore the interaction between in less electron-filling correlated electrons aimed at inducing an ordered superlattice formation, which may be feasible in further research.

Acknowledgments

This project was supported by the National Key R&D Program of China (MOST) (Grant No. 2023YFA1406500, 2018YFE0202700), the National Natural Science Foundation of China (NSFC) (No. 21622304, 61674045, 11604063, 11974422, 12104504), the Strategic Priority Research Program (Chinese Academy of Sciences, CAS) (No. No. XDB30000000). Z. H. Cheng was supported by the Fundamental Research Funds for the Central Universities and the Research Funds of Renmin University of China [No. 21XNLG27, No. 22XNH095].

Author contributions

H.D., Y.G., L.L. and Z.C. performed the STM experiments and analysis of STM data. J.G., M.W., Y.L., L.H., F.P. and R.X. helped in the experiments. W.Z. provided the sample. W.J., H.G., W.Z. and Z.C. wrote the manuscript with inputs from all authors.

Competing Interests

The authors declare no competing financial interests.

Data Availability

The authors declare that the data supporting the findings of this study are available within the article and its Supplementary Information.

Materials and Methods

Single crystal growth of Ti-doped 1T-TaS₂.

The high-quality 1T-Ta_{1-x}Ti_xS₂ bulk single-crystals were grown by chemical vapor transport (CVT) method. Ta (99.99%, Aladdin), TaCl₅ (99.99%, Aladdin), S (99.99%, Aladdin), and Ti (99.99%, Aladdin) powders with a nominal molar ratio of 1:0.02:2.05:x (x = 0.3%, 0.8%, 2.5%, 4.2%, 6.3%) were mixed thoroughly and then loaded into quartz tubes (inner diameter/outer diameter/length: 14/16/200 mm). 0.15 g iodine (~5 mg/cm³) was added into the quartz tube as transport agent. The quartz tubes were sealed under high vacuum of 1.33×10^{-3} Pa and then heated in a two-zone furnace for 7 days, where the temperatures of source and growth zones were kept at 960 °C and 860 °C respectively. The quartz tubes were removed quickly from the furnace and quenched into ice water to obtain the 1T phase. Large 1T-Ta_{1-x}Ti_xS₂ crystals with size up to 10 mm were collected for further characterization and measurement. X-ray diffraction (XRD), scanning electron microscopy (SEM), X-ray energy dispersive spectroscopy (EDS) were employed to determine the crystal structure, morphology, and composition of as-prepared samples. The Ti doping contents of all samples agree with their nominal molar ratio of source materials, demonstrating the controllable synthesis.

Scanning tunneling microscopy (STM).

High-quality Ti-doped 1T-TaS₂ crystals were cleaved at room temperature in ultrahigh vacuum at a base pressure of 2×10^{-10} Torr, and directly transferred to the cryogen-free variable-temperature STM system (PanScan Freedom, RHK). Chemically etched W tips were used for STM measurement in constant-current mode. The tips were calibrated on a clean Ag(111) surface. Gwyddion was used for STM data analysis. The attempt to utilize scanning tunneling spectroscopy (STS) on the intermediate ring-SoD clusters and nematic CDW state has not obtained clear results, as the thermal broadening effect of approximately 50 K and the inherent instability of the tip at this temperature.

References:

1. Han G.H., *et al.* Van der Waals metallic transition metal dichalcogenides. *Chem. Rev.* **118** (13):6297-6336 (2018).
2. Manzeli S., *et al.* 2D transition metal dichalcogenides. *Nat. Rev. Mater.* **2** (8):17033 (2017).
3. Tan C.L., *et al.* Recent advances in ultrathin two-dimensional nanomaterials. *Chem. Rev.* **117** (9):6225-6331 (2017).
4. Bao C. H., Distinguishing and controlling Mottness in 1T-TaS₂ by ultrafast light. *Phys. Rev. B* **107**, L121103 (2023).
5. Ohta S., *et al.* Electronic state modulation of the Star of David lattice by stacking of $\sqrt{13} \times \sqrt{13}$ domains in 1T-TaSe₂. *Phys. Rev. B* **104**, 155433 (2021).
6. Wang Z.L., *et al.* Flat band in hole-doped transition metal dichalcogenide observed by angle-resolved photoemission spectroscopy. *Chin. Phys. B* **32**, 067103 (2023).
7. Nakata Y., *et al.* Robust charge-density wave strengthened by electron correlations in monolayer 1T-TaSe₂ and 1T-NbSe₂. *Nat. Commun.* **12**, 5873 (2021).
8. Lee S., Origin of the insulating phase and first-order metal-insulator transition in 1T-TaS₂. *Phys. Rev. Lett.* **122**, 106404 (2019).
9. Wilson, J.A., *et al.* Charge-density waves in metallic, layered, transition-metal dichalcogenides. *Phys. Rev. Lett.* **32**, 882-885 (1974).
10. Geng Y.Y., *et al.* Hysteretic electronic phase transitions in correlated charge-density-wave state of 1T-TaS₂. *Phys. Rev. B* **107** 195401 (2023).
11. Sipoš B., *et al.* From Mott state to superconductivity in 1T-TaS₂. *Nat. Mater.* **7**, 960-965 (2008).
12. Liu L.W., *et al.* Direct identification of Mott Hubbard band pattern beyond charge density wave superlattice in monolayer 1T-NbSe₂. *Nat. Commun.* **12**, 1978 (2021).
13. Dong H.Y., *et al.* Emergent electron-based Kagome lattice in correlated charge-density-wave state of 1T-TaS₂. *arXiv*: 2301.05885 (2023).
14. Rossnagel, K. & Smith, N.V., Spin-orbit coupling in the band structure of reconstructed 1T-TaS₂. *Phys. Rev. B* **73**, 073106 (2006).
15. Law, K.T. & Lee, P.A., 1T-TaS₂ as a quantum spin liquid. *Proc. Natl. Acad. Sci.* **114**, 6996-7000 (2017).
16. Klanjšek, *et al.* A high-temperature quantum spin liquid with polaron spins. *Nat. Phys.* **13**, 1130-1134 (2017).
17. Ruan W., *et al.* Evidence for quantum spin liquid behaviour in single-layer 1T-TaSe₂ from scanning tunnelling microscopy. *Nat. Phys.* **17**, 1154-1161 (2021).
18. Cho D., *et al.* Nanoscale manipulation of the Mott insulating state coupled to charge order in 1T-TaS₂. *Nat. Commun.* **7**, 10453 (2016).
19. Cho D., *et al.* Correlated electronic states at domain walls of a Mott-charge-density-wave insulator 1T-TaS₂. *Nat. Commun.* **8**, 392 (2017).
20. Ma L., *et al.* A metallic mosaic phase and the origin of Mott-insulating state in 1T-TaS₂. *Nat. Commun.* **7**, 10956 (2016).
21. Karpov P., *et al.* Modeling of networks and globules of charged domain walls observed in pump and pulse induced states. *Sci. Rep.* **8**, 4043 (2018).
22. Mihailovic D., The importance of topological defects in photoexcited phase transitions including memory applications. *Appl. Sci.* **9**, 890 (2019).
23. Park J.W., *et al.* Zoology of domain walls in quasi-2D correlated charge density wave of 1T-TaS₂. *NPJ Quantum Mater.* **6**, 32 (2021).

24. Skolimowski J., *et al.* Mottness collapse without metallization in the domain wall of the triangular-lattice Mott insulator $1T$ -TaS₂. *Phys. Rev. Lett.* **122**, 036802 (2019).
25. Li Y., *et al.* Electronic states of domain walls in commensurate charge density wave ground state and mosaic phase in $1T$ -TaS₂. *Chin. Phys. B* **32**, 077101 (2023).
26. Kranjec A., *et al.* Electronic dislocation dynamics in metastable Wigner crystal states. *Symmetry* **14**,926 (2022).
27. Yao Q.Y., *et al.* Kinkless electronic junction along one dimensional electronic channel. *arXiv:2309.01648* (2023).
28. Song X., *et al.* Atomic-scale visualization of chiral charge density wave superlattices and their reversible switching. *Nat. Commun.* **13**, 1843 (2022).
29. Xi X.X., *et al.* Electronical switching of ferro-rotational order in nanometer-thick $1T$ -TaS₂ crystals. *Nat. Nanotech.* **18** 854-860 (2023).
30. Bediako D.K., *et al.* Encoding multistate charge order and chirality in endotaxial heterostructures. *Nat. Commun.* **14**, 6031 (2023).
31. Liu L.W., *et al.* Unveiling electronic behaviors in heterochiral charge-density-wave twisted stacking materials with 1.25 nm unit dependence. *ACS Nano* **17**,2702-2710 (2023).
32. Zong A., *et al.* Ultrafast manipulation of mirror domain walls in a charge density wave. *Sci. Adv.* **4**, eaau5501 (2018).
33. Mraz A., *et al.* Manipulation of fractionalized charge in the metastable topologically entangled state of a doped Wigner crystal. *Nat. Commun.* **14**, 8214 (2023).
34. Cho D., *et al.* Charge density wave surface reconstruction in a Van der Waals layered material. *Nat. Commun.* **14**, 5735 (2023).
35. Butler C.J., *et al.* Mottness versus unit-cell doubling as the driver of the insulating state in $1T$ -TaS₂. *Nat. Commun.* **11**, 2477 (2020).
36. Butler C.J., *et al.* Doublonlike excitations and their phononic coupling in a Mott charge-density-wave system. *Phys. Rev. X* **11**, 011059 (2021).
37. Zou X.L., *et al.* Probing complex stacking in a layered material via electron-nuclear quadrupolar coupling. *Phys. Rev. Lett.* **7**, L091001 (2023).
38. Pizarro J.M., *et al.* Deconfinement of Mott localized electrons into topological and spin-orbit-coupled Dirac fermions. *NPJ Quantum Mater.* **5**, 79 (2020).
39. Ritschel T., Berger H., Geck J., Stacking-driven gap formation in layered $1T$ -TaS₂. *Phys. Rev. B* **98**, 195134 (2018).
40. Lee J., *et al.* Distinguishing a Mott insulator from a trivial insulator with atomic adsorbates. *Phys. Rev. Lett.* **126**,196405 (2021)
41. Yao Q., *et al.* Engineering domain wall electronic states in strongly correlated van der Waals material of $1T$ -TaS₂. *Nano Lett.* **21**, 9699-9705 (2021).
42. Jarc G., *et al.* Cavity-mediated thermal control of metal-to-insulator transition in $1T$ -TaS₂. *Nature* **622** 487 (2023).
43. Naik G.V., *et al.* Reorganization of CDW stacking in $1T$ -TaS₂ by an in-plane electrical bias. *APL Mater.* **9** 111103 (2021).
44. Gerasimenko Y.A., *et al.* Intertwined chiral charge orders and topological stabilization of the light-induced state of a prototypical transition metal dichalcogenide. *NPJ Quantum Mater.* **4**, 32 (2019).
45. Zhang J., *et al.* Photoexcitation induced quantum dynamics of charge density wave and emergence of a collective mode in $1T$ -TaS₂. *Nano Lett.* **19** 6027-6034 (2019).

46. Gerasimenko Y.A., *et al.* Quantum jamming transition to a correlated electron glass in 1T-TaS₂. *Nat. Mater.* **18** 1078-1083 (2019).
47. Gao J.J., *et al.* Chiral charge density waves induced by Ti-doping in 1T-TaS₂. *Appl. Phys. Lett.* **118**, 213105 (2021).
48. Ravnik J., *et al.* Chiral domain dynamics and transient interferences of mirrored superlattices in nonequilibrium electronic crystals. *Sci. Rep.* **13**:19622 (2023).
49. Zhang Q., *et al.* Bandgap renormalization and work function tuning in MoSe₂/hBN/Ru(0001) heterostructures. *Nat. Commun.* **7**, 13843 (2016).
50. Craes F., *et al.* Mapping image potential states on Graphene quantum dots. *Phys. Rev. Lett.* **111**, 056804 (2013).
51. Liu S., *et al.* Plasmon-assisted resonant electron tunneling in a scanning tunneling microscope junction. *Phys. Rev. Lett.* **121**, 226802 (2018).
52. Werner W.S.M., *et al.* Scanning tunneling microscopy in the field-emission regime: Formation of a two-dimensional electron cascade. *Appl. Phys. Lett.* **115**, 251604 (2019).
53. Schulz F., *et al.* Epitaxial hexagonal boron nitride on Ir(111): A work function template. *Phys. Rev. B* **89**, 235429 (2014).
54. Zhang H.Y., *et al.* Kelvin probe force microscopy study on chiral superconductor 4Hb-TaS₂. *Chin. J. Vac. Sci. Technol.* **43**(10) 825 (2023).